



**HAL**  
open science

## Heterogeneous habenular neuronal ensembles during selection of defensive behaviors

Salvatore Lecca, Vijay Mk Namboodiri, Leonardo Restivo, Nicolas Gervasi, Giuliano Pillolla, Garret D Stuber, Manuel Mameli

► **To cite this version:**

Salvatore Lecca, Vijay Mk Namboodiri, Leonardo Restivo, Nicolas Gervasi, Giuliano Pillolla, et al.. Heterogeneous habenular neuronal ensembles during selection of defensive behaviors. *Cell Reports*, 2020, 31 (10), pp.107752. 10.1016/j.celrep.2020.107752 . hal-04046921

**HAL Id: hal-04046921**

**<https://hal.science/hal-04046921>**

Submitted on 27 Mar 2023

**HAL** is a multi-disciplinary open access archive for the deposit and dissemination of scientific research documents, whether they are published or not. The documents may come from teaching and research institutions in France or abroad, or from public or private research centers.

L'archive ouverte pluridisciplinaire **HAL**, est destinée au dépôt et à la diffusion de documents scientifiques de niveau recherche, publiés ou non, émanant des établissements d'enseignement et de recherche français ou étrangers, des laboratoires publics ou privés.

1 **Heterogeneous habenular neuronal ensembles during selection of**  
2 **defensive behaviors**

3 Salvatore Lecca<sup>1</sup>, Vijay MK Namboodiri<sup>2</sup>, Leonardo Restivo<sup>1</sup>, Nicolas  
4 Gervasi<sup>3</sup>, Giuliano Pillolla<sup>4</sup>, Garret D. Stuber<sup>2</sup> and Manuel Mameli<sup>1,5</sup>

5

6

7 <sup>1</sup> The Department of Fundamental Neuroscience, The University of Lausanne  
8 1005 Lausanne, Switzerland.

9 <sup>2</sup> Center for the Neurobiology of Addiction, Pain, and Emotion, Department of  
10 Anesthesiology and Pain Medicine, Department of Pharmacology, University  
11 of Washington, Seattle, WA, USA.

12 <sup>3</sup> College de France, Inserm, 75005 Paris, France.

13 <sup>4</sup> The University of Cagliari, Cagliari, Italy.

14 <sup>5</sup> Inserm, UMR-S 839, 75005 Paris, France.

15

16 To whom correspondence should be addressed, Lead contacts:

17 Manuel Mameli, PhD

18 Salvatore Lecca, PhD

19 The Department of Fundamental Neuroscience, The University of Lausanne  
20 1005 Lausanne, Switzerland.

21 Email [manuel.mameli@unil.ch](mailto:manuel.mameli@unil.ch), [salvatore.lecca@unil.ch](mailto:salvatore.lecca@unil.ch)

22

23

24

25

26 **Competing financial interests**

27 The authors declare no competing financial interests.

28

29 **Keywords**

30 Lateral habenula, defensive behaviors, single cell calcium imaging in vivo,

31 aversion.

32

33

34

35

36

37

38

39

40

41

42

43

44

45

46

47

48

49

50

51 **Abstract**

52 Optimal selection of threat-driven defensive behaviors is paramount to an  
53 animal's survival. The lateral habenula (LHb) is a key neuronal hub  
54 coordinating behavioral responses to aversive stimuli. Yet, how individual LHb  
55 neurons represent defensive behaviors in response to threats remains  
56 unknown. Here we show that, in mice, a visual threat promotes distinct  
57 defensive behaviors, namely runaway (escape) and action-locking (immobile-  
58 like). Fiber photometry of bulk LHb neuronal activity in behaving animals  
59 revealed an increase and decrease of calcium signal time-locked with  
60 runaway and action-locking, respectively. Imaging single-cell calcium  
61 dynamics across distinct threat-driven behaviors identified independently  
62 active LHb neuronal clusters. These clusters participate during specific time  
63 epochs of defensive behaviors. Decoding analysis of this neuronal activity  
64 unveiled that some LHb clusters either predict the upcoming selection of the  
65 defensive action or represent the selected action. Thus, heterogeneous  
66 neuronal clusters in LHb predict or reflect the selection of distinct threat-driven  
67 defensive behaviors.

68

69

70

71

72

73

## 74 **Introduction**

75 When facing an external threat, animals select from a repertoire of innate  
76 behavioral responses ranging from escape (runaway) to immobile-like (action-  
77 locking) strategies (Evans et al., 2019). These behaviors ultimately increase  
78 individual survival, rely on the external environment, and can be adopted by  
79 the same animal (De Franceschi et al., 2016; Eilam, 2005). The detection of a  
80 threat and the optimal selection of such threat-driven actions (i.e. runaway or  
81 action-locking) require the coordination of complex brain networks. The recent  
82 analysis of threat-driven escape behaviors unraveled the essential  
83 contribution of neuronal circuits including the amygdala, the superior  
84 colliculus, the periaqueductal grey, the hypothalamus or the midbrain. All of  
85 these are pivotal neuronal nodes for aversive processing (Evans et al., 2018;  
86 Headley et al., 2019; Silva et al., 2016; Tovote et al., 2016; Zhou et al., 2019).  
87 Neurons located in the epithalamic lateral habenula (LHb) signal the negative  
88 valence of a stimulus contributing to aversive behaviors (Matsumoto and  
89 Hikosaka, 2007). Accordingly, habenular neurons in fish, rodents and non-  
90 human primates, as opposed to midbrain dopamine neurons, respond mainly  
91 with an excitation to a variety of aversive stimuli, and reduce their activity after  
92 reward presentation (Andalman et al., 2019; Lecca et al., 2017; Matsumoto  
93 and Hikosaka, 2007; Wang et al., 2017). Specifically, aversion-driven LHb  
94 neuronal excitation requires hypothalamic glutamate release to shape  
95 behavioral responses upon unexpected and predicted aversive events  
96 (Lazaridis et al., 2019; Lecca et al., 2017; Trusel et al., 2019). Indeed,  
97 reducing the efficacy of hypothalamus-to-LHb projections impairs behavioral  
98 escape driven by foot shocks, shock-predicting cues and predator-like

99 looming stimulus (Lecca et al., 2017; Trusel et al., 2019). The latter evidence  
100 indicates a relevant contribution of LHb in encoding environmental threats.  
101 Yet, whether specific neuronal representations in the LHb participate in the  
102 selection of threat-driven defensive behaviors (runaway or action-locking),  
103 remains unknown.

104

105 To examine this question, we performed deep-brain Ca<sup>2+</sup>-imaging of large  
106 LHb neuronal populations using a head-mounted miniaturized microscope in  
107 mice engaging visual threat-driven defensive responses (Resendez et al.,  
108 2016). We combined such large-scale recordings with unsupervised  
109 classification of response patterns. This led to the identification of functionally  
110 distinct LHb neuronal subpopulations during threat-driven runaway and  
111 action-locking. Analysis of responses indicates that multiple neuronal clusters  
112 emerge during behavioral strategies holding independent information (i.e.  
113 prediction vs action) related to the temporal expression of the behaviors.  
114 Altogether, these data support the participation of LHb neuronal populations in  
115 the selection of defensive behaviors when facing an external threat.

116

## 117 **Results**

### 118 **Opposing behavioral strategies in response to a visual threat**

119 Ethological studies posit a relationship between the animal-nest distance and  
120 the strategy adopted to react to a threat. The closer to a nest, the more likely  
121 it is for animals to rapidly runaway to hide. Action-locking responses, instead,  
122 occur with higher frequency when the animal is located far from the shelter  
123 (Yilmaz and Meister, 2013).

124 Here we investigated these independent threat-driven behavioral strategies in  
125 mice using an innately aversive overhead expanding spot (Looming) (Yilmaz  
126 and Meister, 2013), while mice explore an experimental arena provided with a  
127 nest. We randomly triggered the looming stimulus when the mouse explored  
128 different zones of the arena with variable distance with respect to the nest  
129 (Figure 1A and B). Mice predominantly adopted threat-driven high-speed  
130 runaway responses (Figure 1A-D). In a smaller fraction of trials, however, the  
131 same animals engaged in a looming-driven action-locking, a behavior outlined  
132 by significant speed reduction (Figure 1A-D). Such opposite threat-driven  
133 behavioral strategies related to the distance from the nest (Figure 1D).  
134 Multiple looming presentations (maximum of 12) revealed comparable  
135 average onset time between runaway and action-locking responses, yet  
136 different offset timing, with action-locking events lasting up to tens of seconds  
137 (Figure 1E). Altogether, mice can display divergent defensive behaviors to the  
138 same visual threat stimulus in a context-dependent fashion.

139

#### 140 **Threat encoding in the lateral habenula**

141 We next employed fiber photometry to measure fluorescent calcium transients  
142 ( $\text{Ca}^{2+}$ ; (Cui et al., 2014)) and examined the population dynamics of LHb  
143 neurons in freely behaving mice (Figure 2A). We injected rAAV2.5-hSyn1-  
144 GCaMP6f into the LHb and implanted an optical fiber above the injection site  
145 (Figure 2A and Figure 2– figure supplement 1A ). The onset of threat-driven  
146 runaway occurred along with a robust increase in  $\text{Ca}^{2+}$  fluorescence from LHb  
147 neurons (Figure 2A, B and movie 1). In contrast, looming-driven action-locking  
148 developed together with a significant reduction in LHb fluorescence (Figure

149 2A, B and movie 2). Notably, a significant shift in fluorescence emerged time-  
150 locked with the visual looming stimulus and prior the behavior (Figure 2–figure  
151 supplement 1B, C). The magnitude of this fluorescence rise was comparable  
152 between runaway and action-locking trials (Figure 2–figure supplement 1B,  
153 C). The observation that no fluorescence transients occurred in animals  
154 injected only with a rAAV2.5-hSyn1-GFP, supports the specificity of signal  
155 detection (Figure 2–figure supplement 2A, B). Both runaway and action-  
156 locking expressed along with an abrupt change in speed at the behavioral  
157 onset (Figure 1C). However, speed changes outside the looming presentation  
158 did not coincide with fluorescence transients, supporting that spontaneous  
159 locomotion does not engage LHb activity (Figure 2–figure supplement 3A, B;  
160 (Lecca et al., 2017)). Altogether, these data suggest that a threat recruits  
161 differential LHb neuronal responses throughout the expression of diverse  
162 behavioral strategies (i.e. from stimulus detection to action completion).

163

#### 164 **Heterogeneity of habenular neuronal activity emerges during defensive** 165 **behaviors**

166 Analysis of neuronal function with fiber photometry (Figure 2A, B) lacks  
167 cellular-level resolution, and provides only aggregated activity from large  
168 neuronal populations (Resendez et al., 2016). Such limitation can be  
169 circumvented through the use of gradient-refractive-index (GRIN) lenses,  
170 which enable visualization of deep-brain neuronal activity with single-cell  
171 resolution. We next examined how individual LHb neurons represent threats  
172 via their activity patterns. We used a miniature fluorescence microscope to  
173 track the relative changes in Ca<sup>2+</sup> fluorescence in LHb neurons in freely



174 moving mice during threat-driven behaviors (Figure 3A;  $62 \pm 14.6$  neurons per  
175 animal;  $n_{\text{mice}} = 4$ ). Lhb neurons exhibited diverse activity patterns, with sharp  
176 elevations in  $\text{Ca}^{2+}$  fluorescence during runaway. The response was in the  
177 opposite direction during action-locking trials (Figure 3B and Figure 3–figure  
178 supplement 1A). The average  $\text{Ca}^{2+}$  signal across all neurons recorded from a  
179 single animal recapitulated the response profiles observed with photometric  
180 analysis, supporting the validity of these experimental approaches (Figure 3B,  
181 Figure 3–figure supplement 1A and Figure 2B). Thus, single cell analysis of  
182  $\text{Ca}^{2+}$  signal indicates that opposite neuronal responses in the Lhb reflect  
183 independent threat-driven behavioral strategies.

184

185 Individual Lhb cells displayed variable profiles of runaway-excited/action-  
186 locking inhibited responses (Figure 3–figure supplement 1A, B). Furthermore,  
187 the activity of single neurons during a given defensive strategy across trials  
188 was also variable (Figure 3–figure supplement 1C). Altogether, this argues in  
189 favor of functional heterogeneity across Lhb neuronal responses after threat.  
190 We thereby used an unsupervised clustering algorithm to group the trial-  
191 averaged time-locked response of each cell after runaway and action-locking  
192 onset ( $n = 248$  from  $n = 4$  mice; Figure 3C and Figure S4A). This analysis  
193 revealed eight clusters of neurons based on their responses surrounding the  
194 behavioral onset (Figure 3C, Figure 3–figure supplement 2A, B). Clusters  
195 were represented in each animal, supporting the strength of independent  
196 neuronal representations (Figure 3–figure supplement 2C). The responses of  
197 clusters 1 to 5, qualitatively recapitulated fiber photometry  $\text{Ca}^{2+}$  dynamics  
198 time-locked to runaway and action-locking onset (Figure 3C). Cluster 7 and 8,

199 instead, were weakly modulated during looming-triggered defensive  
200 responses. Interestingly, Clusters 3 and 6 stood out as their pre-action  $\text{Ca}^{2+}$   
201 dynamics discriminated the upcoming behavior (Figure 3C). Altogether, this  
202 supports the existence of distinct clusters of individual neurons participating  
203 throughout threat-driven behavioral responses.

204

### 205 **Decoding the contribution of habenular clusters to threat-driven** 206 **behaviors**

207 The existence of clusters with neuronal activity that distinguishes the  
208 defensive behaviors *prior* to the onset of the action (especially 3 and 6)  
209 raised the intriguing possibility that LHb neurons may predict the upcoming  
210 selection of runaway or action-locking. To test this idea, we examined the  
211 neuronal coding of LHb ensembles by testing whether the defensive strategy  
212 on a given trial was identifiable from individual neuron activity patterns (Figure  
213 4A). We defined three time epochs as “prediction of action” (-3 to 0 s from  
214 action), “immediate action” (0 to 3 s from action), and “delayed action” (3 to 6  
215 s from action) (Figure 4B). Using leave-one-out cross-validation of a Naïve  
216 Bayes classifier (Namboodiri et al., 2019), we calculated the decoding  
217 accuracy per neuron above the chance decoding obtained when shuffling trial  
218 identity. We then averaged these accuracies across all recorded neurons  
219 (Figure 4C) or across all neurons within a cluster (Figure 4D). The null  
220 hypothesis was that the average decoding accuracy (above chance) per  
221 timeframe and (sub)population is zero. We found that the average decoding  
222 accuracy across all recorded neurons was significant for each time epoch  
223 (Figure 4C). Interestingly, decoding accuracies showed cluster-specific

224 patterns. Most notably, we found that clusters 3 and 6 showed significant  
225 decoding (after correcting for multiple comparison) during the “prediction of  
226 action” epoch, whereas other clusters (also including cluster 3) showed  
227 significant decoding after the action (Figure 4D). Matching the cluster identity  
228 with the topographical neuronal localization during the recordings, revealed  
229 that the clusters related to prediction, (clusters 3 and 6), were located caudally  
230 with respect to the rest of the clusters (Figure 3–figure supplement 2D).  
231 Overall, these results demonstrate that distinct neuronal subpopulations within  
232 the LHb either predict or reflect defensive behavioral selection in response to  
233 a threat.

234

## 235 **Discussion**

### 236 **Dissecting specific contribution of LHb activity for aversion**

237 The past decade witnessed exponentially growing interest in the essential role  
238 the LHb has in regulating negatively motivated behaviors. It is of a general  
239 consensus within the field that LHb neurons are a homogenous population of  
240 glutamatergic cells mostly controlling the function of neuromodulatory systems  
241 (Meye et al., 2013). It is also largely accepted that LHb neurons are uniformly  
242 excited by aversive external stimuli (Lecca et al., 2017; Matsumoto and  
243 Hikosaka, 2007; Wang et al., 2017). Here, we challenge this vision of  
244 homogeneity showing that in response to an identical aversive stimulus (the  
245 looming), LHb cells dynamics follow opposite logic in a behavior-dependent  
246 manner: an escape reaction (runaway) recruits mainly an activation of LHb  
247 cells. In contrast, action-locking responses occur along with a decrease in  
248 calcium activity, potentially reflecting neuronal inhibition (Namboodiri et al.,

249 2019; Shabel et al., 2019; Wang et al., 2017). Accordingly, aversive foot-  
250 shock inhibited neuronal activity of a small and territorially distinct subset of  
251 LHb cells (Congiu et al., 2019). Based on this, future work should avoid  
252 generalizing that LHb contribution to aversion encoding solely relates to its  
253 excitation. Notably, the opposite responses emerging after the looming can  
254 occur within the same neuron. It is therefore plausible that a given external  
255 stimulus drives dissimilar responses in single cells. The substrate (i.e.  
256 connectivity or gene) enabling such neuronal population to encode both  
257 behavioral aspects remains however an open question.

258

### 259 **Functional heterogeneity in LHb for threat-driven behaviors**

260 On the basis of recordings and analysis of around 250 LHb cells while  
261 animals experience a threat, here we show how ensembles of neurons  
262 represent threat-driven behavioral defensive strategies. An unsupervised  
263 clustering reveals that independent sets of active neurons form during the  
264 expression of threat-mediated behavioral responses (Gründemann et al.,  
265 2019; Namboodiri et al., 2019). Such discrete neuronal clusters are stable and  
266 define timeframes of threat detection and behavioral action (Gründemann et  
267 al., 2019). It remains unclear however which neurobiological substrate defines  
268 LHb clusters. Within the amygdala and the cortex, genetically distinct  
269 neuronal subtypes contribute to different phases of adaptive behaviors (Abs et  
270 al., 2018; Douglass et al., 2017; Krabbe et al., 2019). Recent studies identified  
271 molecular-level neuronal diversity within the LHb (Wallace et al., 2019;  
272 Hashikawa et al., 2019). Exploiting this genetic knowledge may provide an  
273 entry point to specifically probe the functional and behavioral relevance of

274 individual LHb neuronal clusters identified in this study. Alternative to a  
275 genetic basis, clusters may emerge according to topographical organization,  
276 input-specific connectivity or discrete projection targets (Cerniauskas et al.,  
277 2019; Lecca et al., 2017; Meye et al., 2016; Shabel et al., 2012; Valentinova  
278 et al., 2019). Our analysis indicates that some LHb neuronal clusters are  
279 topographically distinct. This heightens the need of future studies to address  
280 this unresolved questions. Notably, the multilevel heterogeneity (functional,  
281 anatomical, molecular) emerging lately replaces the initial uniform connotation  
282 attributed to the LHb. Further studies will need to determine the relationship  
283 across these multiple levels of heterogeneity and establish their behavioral  
284 relevance.

285

### 286 **Complex neuronal networks for defensive behaviors**

287 The initial observation that limiting excitation onto LHb impairs escape  
288 behaviors implicated this structure in the encoding of innate escape (Lecca et  
289 al., 2017). An original aspect of the present work lies on the demonstration  
290 that LHb activity changes when animals escape or action-lock after looming  
291 presentation. In contrast, recent studies support the contribution of several  
292 midbrain nuclei mostly for threat-driven escape (Evans et al., 2018; Seo et al.,  
293 2019). Indeed, Ca<sup>2+</sup> imaging and brain circuit manipulation approaches  
294 demonstrate that glutamatergic neurons of the dorsal periaqueductal grey  
295 encode decision making and escape (Evans et al., 2018). In addition, a visual  
296 pathway engaging superior colliculus and amygdala also contributes to  
297 defensive strategies (Shang et al., 2018). Finally, GABAergic neurons in the  
298 ventral tegmental area (VTA) projecting to the central amygdala (CeA) seem

299 to be similarly instrumental for threat-driven escape responses (Zhou et al.,  
300 2019). Intriguingly, LHb axons innervate these VTA-GABA cells projecting to  
301 CeA. Future studies should test how diverse defensive strategies engage  
302 wide interconnected networks activity to ultimately build an integrated  
303 framework for threat-driven behavioral responses. Defensive strategies are a  
304 combination of behavioral sets relying on unique features including  
305 trajectories, or stereotyped movements (Evans et al., 2019). The use of deep  
306 neural network analysis tracking facets of animal behaviors (Nath et al., 2019;  
307 Wiltschko et al., 2015) may pave the way to differentiate precise aspects of  
308 defensive behaviors. This will allow a refined alignment with the neuronal  
309 dynamics in defined neuronal circuits (Klaus et al., 2017).

310

311 The relationship between LHb function and optimal selection of defensive  
312 strategies remains correlative after the analysis of the photometric signal. Yet,  
313 the unsupervised clustering and decoding analysis support: *i.* that LHb activity  
314 codes for distinct behavioral strategies, *ii.* that the dynamics of discrete LHb  
315 neuronal clusters reflect precise time epochs of defensive behaviors and *iii.*  
316 that these clusters can predict upcoming selection of the action or represent  
317 an action itself (Grewe et al., 2017; Namboodiri et al., 2019). Opto or  
318 chemogenetic interrogation of LHb neuronal population offers a mean to  
319 probe causality between neuronal activity and behaviors (Saunders et al.,  
320 2015). However, this intervention is challenging in the present context, as it is  
321 limited by the lack of population-specific viral targeting within LHb (i.e. lack of  
322 genetic tools for LHb diversity). The manipulation of LHb function in a non  
323 cell-specific fashion remains a poor approach to test for causality. This would

324 not fulfill the requirement of precise neuronal cluster targeting, a feature  
325 highlighted in the functional and topographical analysis provided in this work.  
326 The latest insights of genetic profiling may soon provide the tools to assess  
327 these outstanding questions.

328

329 In summary, our results identify the evolution of individual neuronal responses  
330 in a deep structure like the LHb during threat-driven behavioral strategies, an  
331 objective so far proven challenging due to technical difficulties. We  
332 demonstrated that LHb neuronal clusters participate to the optimal selection of  
333 defensive strategies. Future studies can provide a link between this functional  
334 heterogeneity with genetic and anatomical aspects to establish a  
335 comprehensive knowledge of LHb contribution to threat encoding. Altogether,  
336 these findings advance our understanding of the neuronal basis of  
337 ethologically-relevant innate behaviors.

338

### 339 **Contributions**

340 S.L. and M.M. conceptualized the project. S.L. performed and analyzed  
341 behaviors and in vivo calcium imaging. L.R. provided support for behavioral  
342 analysis and experiments. N.G. performed independent calcium imaging  
343 analysis. G.P. provided analytical support for the photometric detection.  
344 V.M.K.N. and G.D.S. provided support, and analysis for calcium imaging  
345 analysis and help in editing the manuscript. M.M. and S.L. wrote the  
346 manuscript with the help of all authors.

347

348

349

350 **Acknowledgements**

351 We thank all the members of the Mameli laboratory for comments on the  
352 manuscript. We thank C. Lüscher, R. Van Zessen, A. Adamantidis, L. Oesch,  
353 J. Zapata, and K. Tan for technical assistance. This work was supported by  
354 the ERC StG SalienSy 335333, the Swiss National Funds 31003A and Vaud  
355 Canton to M.M., the NARSAD Young Investigator to S.L. and V.M.K.N, and  
356 K99MH118422 from US National Institute of Mental Health to V.M.K.N.

357

358



359 **References**

- 360 Abs, E., Poorthuis, R. B., Apelblat, D., Muhammad, K., Pardi, M. B., Enke, L.,  
361 Kushinsky, D., Pu, D. L., Eizinger, M. F., Conzelmann, K. K., Spiegel, I., and  
362 Letzkus, J. J. (2018). Learning-Related Plasticity in Dendrite-Targeting Layer  
363 1 Interneurons. *Neuron* 100, 684-699.e6.
- 364 Andalman, A. S., Burns, V. M., Lovett-Barron, M., Broxton, M., Poole, B.,  
365 Yang, S. J., Grosenick, L., Lerner, T. N., Chen, R., Benster, T., Mourrain, P.,  
366 Levoy, M., Rajan, K., and Deisseroth, K. (2019). Neuronal Dynamics  
367 Regulating Brain and Behavioral State Transitions. *Cell* 177, 970-985.e20.
- 368 Cerniauskas, I., Winterer, J., de Jong, J. W., Lukacsovich, D., Yang, H., Khan,  
369 F., Peck, J. R., Obayashi, S. K., Lilascharoen, V., Lim, B. K., Földy, C., and  
370 Lammel, S. (2019). Chronic Stress Induces Activity, Synaptic, and  
371 Transcriptional Remodeling of the Lateral Habenula Associated with Deficits  
372 in Motivated Behaviors. *Neuron* 104, 899-915.e8.
- 373 Congiu, M., Trusel, M., Pistis, M., Mameli, M., and Lecca, S. (2019). Opposite  
374 responses to aversive stimuli in lateral habenula neurons. *Eur J Neurosci* 50,  
375 2921-2930.
- 376 Cui, G., Jun, S. B., Jin, X., Luo, G., Pham, M. D., Lovinger, D. M., Vogel, S.  
377 S., and Costa, R. M. (2014). Deep brain optical measurements of cell type-  
378 specific neural activity in behaving mice. *Nat Protoc* 9, 1213-1228.
- 379 De Franceschi, G., Vivattanasarn, T., Saleem, A. B., and Solomon, S. G.  
380 (2016). Vision Guides Selection of Freeze or Flight Defense Strategies in  
381 Mice. *Curr Biol* 26, 2150-2154.
- 382 Douglass, A. M., Kucukdereli, H., Ponserre, M., Markovic, M., Gründemann,  
383 J., Strobel, C., Alcalá Morales, P. L., Conzelmann, K. K., Lüthi, A., and Klein,

384 R. (2017). Central amygdala circuits modulate food consumption through a  
385 positive-valence mechanism. *Nat Neurosci* 20, 1384-1394.

386 Eilam, D. (2005). Die hard: a blend of freezing and fleeing as a dynamic  
387 defense--implications for the control of defensive behavior. *Neurosci Biobehav*  
388 *Rev* 29, 1181-1191.

389 Evans, D. A., Stempel, A. V., Vale, R., and Branco, T. (2019). Cognitive  
390 Control of Escape Behaviour. *Trends Cogn Sci* 23, 334-348.

391 Evans, D. A., Stempel, A. V., Vale, R., Ruehle, S., Lefler, Y., and Branco, T.  
392 (2018). A synaptic threshold mechanism for computing escape decisions.  
393 *Nature* 558, 590-594.

394 Grewe, B. F., Gründemann, J., Kitch, L. J., Lecoq, J. A., Parker, J. G.,  
395 Marshall, J. D., Larkin, M. C., Jercog, P. E., Grenier, F., Li, J. Z., Lüthi, A., and  
396 Schnitzer, M. J. (2017). Neural ensemble dynamics underlying a long-term  
397 associative memory. *Nature* 543, 670-675.

398 Gründemann, J., Bitterman, Y., Lu, T., Krabbe, S., Grewe, B. F., Schnitzer, M.  
399 J., and Lüthi, A. (2019). Amygdala ensembles encode behavioral states.  
400 *Science* 364,

401 Hashikawa Y., Hashikawa K., Basiri M.L., Liu Y., Johnston N.L., Ahmad O.R.,  
402 Stuber G.D.. Transcriptional and spatial resolution of cell types in the  
403 mammalian habenula. *BiorXiv preprint* doi: <https://doi.org/10.1101/772376>.

404

405 Headley, D. B., Kanta, V., Kyriazi, P., and Paré, D. (2019). Embracing  
406 Complexity in Defensive Networks. *Neuron* 103, 189-201.

407 Klaus, A., Martins, G. J., Paixao, V. B., Zhou, P., Paninski, L., and Costa, R.  
408 M. (2017). The Spatiotemporal Organization of the Striatum Encodes Action  
409 Space. *Neuron* 96, 949.

410 Krabbe, S., Paradiso, E., d'Aquin, S., Bitterman, Y., Courtin, J., Xu, C.,  
411 Yonehara, K., Markovic, M., Müller, C., Eichlisberger, T., Gründemann, J.,  
412 Ferraguti, F., and Lüthi, A. (2019). Adaptive disinhibitory gating by VIP  
413 interneurons permits associative learning. *Nat Neurosci* 22, 1834-1843.

414 Lazaridis, I., Tzortzi, O., Weglage, M., Martin, A., Xuan, Y., Parent, M.,  
415 Johansson, Y., Fuzik, J., Fürth, D., Fenno, L. E., Ramakrishnan, C.,  
416 Silberberg, G., Deisseroth, K., Carlén, M., and Meletis, K. (2019). A  
417 hypothalamus-habenula circuit controls aversion. *Mol Psychiatry* 24, 1351-  
418 1368.

419 Lecca, S., Meye, F. J., Trusel, M., Tchenio, A., Harris, J., Schwarz, M. K.,  
420 Burdakov, D., Georges, F., and Mameli, M. (2017). Aversive stimuli drive  
421 hypothalamus-to-habenula excitation to promote escape behavior. *Elife* 6,  
422 Matsumoto, M., and Hikosaka, O. (2007). Lateral habenula as a source of  
423 negative reward signals in dopamine neurons. *Nature* 447, 1111-1115.

424 Meye, F. J., Lecca, S., Valentinova, K., and Mameli, M. (2013). Synaptic and  
425 cellular profile of neurons in the lateral habenula. *Front Hum Neurosci* 7, 860.

426 Meye, F. J., Soiza-Reilly, M., Smit, T., Diana, M. A., Schwarz, M. K., and  
427 Mameli, M. (2016). Shifted pallidal co-release of GABA and glutamate in  
428 habenula drives cocaine withdrawal and relapse. *Nat Neurosci* 19, 1019-  
429 1024.

430 Namboodiri, V. M. K., Otis, J. M., van Heeswijk, K., Voets, E. S., Alghorazi, R.  
431 A., Rodriguez-Romaguera, J., Mihalas, S., and Stuber, G. D. (2019). Single-

432 cell activity tracking reveals that orbitofrontal neurons acquire and maintain a  
433 long-term memory to guide behavioral adaptation. *Nat Neurosci* 22, 1110-  
434 1121.

435 Nath, T., Mathis, A., Chen, A. C., Patel, A., Bethge, M., and Mathis, M. W.  
436 (2019). Using DeepLabCut for 3D markerless pose estimation across species  
437 and behaviors. *Nat Protoc* 14, 2152-2176.

438 Resendez, S. L., Jennings, J. H., Ung, R. L., Namboodiri, V. M., Zhou, Z. C.,  
439 Otis, J. M., Nomura, H., McHenry, J. A., Kosyk, O., and Stuber, G. D. (2016).  
440 Visualization of cortical, subcortical and deep brain neural circuit dynamics  
441 during naturalistic mammalian behavior with head-mounted microscopes and  
442 chronically implanted lenses. *Nat Protoc* 11, 566-597.

443 Saunders, B. T., Richard, J. M., and Janak, P. H. (2015). Contemporary  
444 approaches to neural circuit manipulation and mapping: focus on reward and  
445 addiction. *Philos Trans R Soc Lond B Biol Sci* 370, 20140210.

446 Seo, C., Guru, A., Jin, M., Ito, B., Slezzer, B. J., Ho, Y. Y., Wang, E., Boada,  
447 C., Krupa, N. A., Kullakanda, D. S., Shen, C. X., and Warden, M. R. (2019).  
448 Intense threat switches dorsal raphe serotonin neurons to a paradoxical  
449 operational mode. *Science* 363, 538-542.

450 Shabel, S. J., Proulx, C. D., Trias, A., Murphy, R. T., and Malinow, R. (2012).  
451 Input to the lateral habenula from the basal ganglia is excitatory, aversive, and  
452 suppressed by serotonin. *Neuron* 74, 475-481.

453 Shabel, S. J., Wang, C., Monk, B., Aronson, S., and Malinow, R. (2019).  
454 Stress transforms lateral habenula reward responses into punishment signals.  
455 *Proc Natl Acad Sci U S A* 116, 12488-12493.

456 Shang, C., Chen, Z., Liu, A., Li, Y., Zhang, J., Qu, B., Yan, F., Zhang, Y., Liu,  
457 W., Liu, Z., Guo, X., Li, D., Wang, Y., and Cao, P. (2018). Divergent midbrain  
458 circuits orchestrate escape and freezing responses to looming stimuli in mice.  
459 *Nat Commun* 9, 1232.

460 Silva, B. A., Mattucci, C., Krzywkowski, P., Cuzzo, R., Carbonari, L., and  
461 Gross, C. T. (2016). The ventromedial hypothalamus mediates predator fear  
462 memory. *Eur J Neurosci* 43, 1431-1439.

463 Tovote, P., Esposito, M. S., Botta, P., Chaudun, F., Fadok, J. P., Markovic,  
464 M., Wolff, S. B., Ramakrishnan, C., Fenno, L., Deisseroth, K., Herry, C.,  
465 Arber, S., and Lüthi, A. (2016). Midbrain circuits for defensive behaviour.  
466 *Nature* 534, 206-212.

467 Trusel, M., Nuno-Perez, A., Lecca, S., Harada, H., Lalive, A. L., Congiu, M.,  
468 Takemoto, K., Takahashi, T., Ferraguti, F., and Mameli, M. (2019).  
469 Punishment-Predictive Cues Guide Avoidance through Potentiation of  
470 Hypothalamus-to-Habenula Synapses. *Neuron* 102, 120-127.e4.

471 Valentinova, K., Tchenio, A., Trusel, M., Clerke, J. A., Lalive, A. L.,  
472 Tzanoulinou, S., Matera, A., Moutkine, I., Maroteaux, L., Paolicelli, R. C.,  
473 Volterra, A., Bellone, C., and Mameli, M. (2019). Morphine withdrawal recruits  
474 lateral habenula cytokine signaling to reduce synaptic excitation and  
475 sociability. *Nat Neurosci* 22, 1053-1056.

476 Wallace M.L., Huang K.W., Hochbaum D., Hyun M., Radeljic G., Sabatini  
477 B.L.. Distinct neuronal subtypes of the lateral habenula differentially target  
478 ventral tegmental area dopamine neurons. *BiorXiv preprint*  
479 doi: <https://doi.org/10.1101/743401>.

480 Wang, D., Li, Y., Feng, Q., Guo, Q., Zhou, J., and Luo, M. (2017). Learning  
481 shapes the aversion and reward responses of lateral habenula neurons. *Elife*  
482 *6*,

483 Wang, L. (2019). A VTA GABAergic Neural Circuit Mediates Visually Evoked  
484 Innate Defensive Responses. *Neuron* *103*, 473-488.e6.

485 Wiltschko, A. B., Johnson, M. J., Iurilli, G., Peterson, R. E., Katon, J. M.,  
486 Pashkovski, S. L., Abaira, V. E., Adams, R. P., and Datta, S. R. (2015).  
487 Mapping Sub-Second Structure in Mouse Behavior. *Neuron* *88*, 1121-1135.

488 Yilmaz, M., and Meister, M. (2013). Rapid innate defensive responses of mice  
489 to looming visual stimuli. *Curr Biol* *23*, 2011-2015.

490 Zhou, Z., Liu, X., Chen, S., Zhang, Z., Liu, Y., Montardy, Q., Tang, Y., Wei, P.,  
491 Liu, N., Li, L., Song, R., Lai, J., He, X., Chen, C., Bi, G., Feng, G., Xu, F., and  
492  
493  
494  
495  
496  
497  
498  
499  
500  
501  
502  
503  
504

505 **Figure legends**

506 **Figure 1. Threat exposure promotes divergent defensive strategies.**

507 (A) Schematic of the looming protocol.

508 (B) Extracted video frames depicting a mouse during looming-driven runaway  
509 (top) and action-locking (bottom).

510 (C) Representative single mouse runaway and action-locking trials to multiple  
511 looming stimuli.

512 (D) Top: representative track of a single mouse during a runaway and an  
513 action-locking trials. Bottom: strategy probability in function of the mouse-nest

514 distance ( $n_{\text{runaway trials}} = 56$ ;  $n_{\text{action-locking trials}} = 23$ ;  $n_{\text{mice}} = 11$ ; *Mouse-nest distance*  
515 (*Max distance = 1*): R trials vs AL trials; 0.3: 4 vs 0; 0.4: 7 vs 0; 0.5: 8 vs 0;

516 0.6: 10 vs 2; 0.7: 11 vs 0; 0.8: 9 vs 6; 0.9: 3 vs 3; 1.0: 4 vs 12;  $X^2_7 = 31.68$ ;

517 \*\*\* $p < 0.0001$ , Chi Square test). The lines fitting a sigmoidal distribution reports  
518 the correlation between the mouse-nest distance and the selected strategy

519 (Runaway:  $r = -0.883$ ,  $R^2 = 0.78$ , \*\* $p = 0.003$ ; Action-locking:  $r = 0.884$ ,

520  $R^2 = 0.78$  \*\* $p = 0.003$ , Pearson correlation coefficient)

521 (E) Left: Single mouse runaway (R, in red) and action-locking (AL, in blue)

522 timeframe reported for each trial (dot: onset response, line: offset response).

523 Right: pooled data ( $n_{\text{runaway trials}} = 56$ ;  $n_{\text{action-locking trials}} = 23$ ) for onset (R vs AL;

524  $1.631 \pm 0.14$  vs  $1.797 \pm 0.34$  s;  $t_{77} = 0.53$ ;  $p = 0.59$ , unpaired t-test) and duration

525 (R vs AL;  $1.52 \pm 0.14$  vs  $9.58 \pm 2.37$  s;  $t_{77} = 5.29$ ; \*\*\* $p < 0.0001$ , unpaired t-test)

526 of runaway and action-locking.

527 Data are presented with boxplots (median and 10-90 quartile) or mean  $\pm$

528 S.E.M.

529

530 **Figure 2. Opposite habenular neuronal dynamics during divergent**  
531 **defensive strategies.**

532 (A) Top: schematic of the experiment. Bottom left: representative brain  
533 coronal section showing GCamp6f transduction and the fiber implantation  
534 track in the LHb. Bottom right: representative  $\text{Ca}^{2+}$  traces during runaway (R,  
535 red, top) and action locking (AL, blue, bottom) trials (Looming, gray bar).  
536 (B) Top, time-course of averaged traces and boxplots reporting respectively  
537 normalized photons (R = 56 trials,  $F_{3850} = 50.88$ ,  $***p < 0.0001$ ; AL=23 trials,  
538  $F_{1540} = 3.642$ ,  $*p = 0.012$ ; RM One way ANOVA) and area under the curve (R vs  
539 AL,  $11.70 \pm 5.95$  vs  $-12.96 \pm 6.85$ ;  $t_{77} = 2.40$ ,  $*p = 0.019$ , Unpaired t-test) for  
540 single trials aligned to the behavioral onset.  
541 Bottom: same as top but aligned to the offset (R:  $F_{3850} = 65.71$ ,  $***p < 0.0001$ ;  
542 AL:  $F_{1540} = 6.79$ ,  $***p < 0.0001$ ; RM One way ANOVA; AUC analysis: R vs AL, -  
543  $42.07 \pm 4.01$  vs  $26.16 \pm 5.71$ ;  $t_{77} = 9.401$ ,  $***p < 0.0001$ , Unpaired t-test).  
544 Data are presented with boxplots (median and 10-90 quartile) or mean  $\pm$   
545 S.E.M.

546

547 **Figure 3. Distinct LHb neuronal ensembles during defensive behaviors**

548 (A) Top: schematic of the experiment. Bottom, pictures showing mouse with  
549 miniscope attached, GRIN lens placement, GCaMP6f expression, field of view  
550 with identified cells (max intensity projections), map of active LHb neurons  
551 and respective sample traces (right).  
552 (B) Mean  $\text{Ca}^{2+}$  responses (z-score) across runaway (left) and action locking  
553 (right) trials for 46 LHb neurons imaged within a single mouse, aligned to the  
554 onset of the behavioral reaction. Highlighted on the top, the average response



555 of a single cell (Cell ID: 15) . Bottom, averaged time-course of all cells for  
556 runaway and action locking strategies.

557 (C) Cluster identification by unsupervised classification during runaway (top)  
558 and action-locking (center) including all neurons recorded. Bottom, average  
559 trace across all neurons within cluster. Plots are aligned to the action onset.  
560

561 **Figure 4. Identified LHb neuronal clusters code for behavioral**  
562 **preparation and execution**

563 (A) Single cell activity across trials during runaway and action locking reported  
564 as heat plots (left) and mean z-score (right). Note, trials are time-locked with  
565 the behavior and presented different onset due to trial by trial variability in  
566 reaction time (blank spaces in the heat plots)

567 (B) Workflow for decoding analysis of single neurons activity. The decoder  
568 was run in three different time epochs (-3 to 0 s, burgundy bar; 0 to 3 s, green  
569 bar; 3 to 6 s yellow bar) relatively to the behavioral onset.

570 (C) Single cell decoding accuracy above chance averaged across all recorded  
571 neurons. Red dots highlights significance above chance. Error bars reflect  
572 standard error of the mean.  $t_{247} = 3.23$  for -3 to 0 s,  $t_{247} = 9.37$  for 0 to 3 s,  $t_{247}$   
573  $= 7.54$  for 3 to 6 s; p values for the three epochs =  $2.67 \times 10^{-3}$ ,  $1.56 \times 10^{-18}$  and  
574  $6.84 \times 10^{-13}$  after Benjamini-Hochberg multiple comparisons correction across  
575 all epochs.

576 (D) Decoding results split by the clusters. Red dots highlights significance  
577 above chance.  $t_{247} = (0.44, 0.12, 2.54, 1.20, 0.35, 2.58, 0.78, 1.94)$  for the 8  
578 clusters for -3 to 0 s,  $t_{247} = (6.62, 5.03, 4.16, 4.20, 2.07, -0.19, 2.25, 4.33)$  for  
579 the 8 clusters for 0 to 3 s,  $t_{247} = (3.13, 8.66, 2.99, 4.43, 3.27, -2.44, 2.42, 1.67)$

580 for the 8 clusters for 3 to 6 s; p values for the three epochs per cluster =  
581  $(7.55 \times 10^{-1}, 9.07 \times 10^{-1}, 2.99 \times 10^{-2}, 2.96 \times 10^{-1}, 7.97 \times 10^{-1}, 2.63 \times 10^{-2}, 5.28 \times 10^{-1},$   
582  $7.91 \times 10^{-2})$  for -3 to 0 s,  $(2.87 \times 10^{-7}, 4.07 \times 10^{-5}, 5.35 \times 10^{-4}, 3.39 \times 10^{-4}, 6.54 \times 10^{-2},$   
583  $4.43 \times 10^{-1}, 4.54 \times 10^{-2}, 1.89 \times 10^{-4})$  for 0 to 3 s, and  $(7.78 \times 10^{-3}, 1.18 \times 10^{-10},$   
584  $1.12 \times 10^{-2}, 1.89 \times 10^{-4}, 5.67 \times 10^{-3}, 9.84 \times 10^{-1}, 3.22 \times 10^{-2}, 1.31 \times 10^{-1})$  for 3 to 6 s  
585 after Benjamini-Hochberg multiple comparisons correction across all clusters  
586 and epochs.  
587  
588  
589  
590

591 **Supplementary figures legends**

592

593 **Figure 2–figure supplement 1. Looming-locked shift in LHb Ca<sup>2+</sup> signal**  
594 **occurs prior runaway and action-locking**

595 (A) Schematic of fiber placement in the LHb (brown rectangles represent fiber  
596 tip placement)

597 (B) Representative averaged traces and boxplots for Runaway (R, 56 trials)  
598 and Action-locking (AL, 23 trials) reporting the slope 0.5 s before the  
599 behavioral onset (R vs AL,  $0.030 \pm 0.012$  vs  $0.032 \pm 0.015$ ,  $t_{77}=0.127$ ,  $p=0.91$   
600 Unpaired t-test)

601 (C) Normalized photon traces and area under curve showing the LHb activity  
602 time-locked with the looming onset for Runaway (51 trials,  $F_{480}= 4.10$ ;  
603  $***p<0.0001$ , RM One way ANOVA) and Action-locking trials (18 trials,  $F_{153}=$   
604  $2.45$ ;  $**p=0.002$ , RM One way ANOVA). Boxplots reported the AUC for the  
605 same set of data (R vs AL,  $0.87 \pm 0.22$  vs  $0.63 \pm 0.15$ ;  $t_{67}= 0.612$ ,  $p=0.54$   
606 Unpaired t-test). Note that for this analysis trials displaying a behavioral onset  
607  $< 0.5$  sec were discarded to avoid behavior-dependent signal contamination.  
608 Data are presented with boxplots (median and 10-90 quartile) or mean  $\pm$   
609 S.E.M.

610

611 **Figure 2–figure supplement 2. Lack of fluorescent transients in absence**  
612 **of GCamp6f expression.**

613 (A) Schematic of the experiment and representative brain coronal section  
614 showing eGFP injections in the LHb ( $n_{mice}= 5$ ).

615 (B) Left: Normalized photons time-course graph showing averaged traces of  
616 Runaway (R,  $n_{\text{trials}}=21$ ,  $F_{1400}=2.46$ ,  $p=0.065$ , RM One way ANOVA) and  
617 Action-locking (AL,  $n_{\text{trials}}=12$ ,  $F_{770}=0.946$ ,  $p=0.401$  RM One way ANOVA)  
618 trials time-locked with the behavioral onset. Right: area under curve (AUC) for  
619 the same data set (R vs AL,  $2.662 \pm 1.96$  vs  $-0.6096 \pm 2.18$ ;  $t_{31}=1.063$ ,  
620  $p=0.295$ , Unpaired t-test).

621 (C) Same as (B) but trials are locked with the offset of the behavior (R:  
622  $F_{1400}=0.83$ ,  $p=0.394$ ; AL:  $F_{770}=0.906$ ,  $p=0.452$ ; RM One way ANOVA. AUC  
623 analysis: (R vs AL,  $1.051 \pm 1.58$  vs  $0.3684 \pm 2.24$ ;  $t_{31}=0.253$ ,  $p=0.801$  Unpaired  
624 t-test).

625 Data are presented with boxplots (median and 10-90 quartile) or mean  $\pm$   
626 S.E.M.

627

628 **Figure 2—figure supplement 3. LHb neuronal  $\text{Ca}^{2+}$  transients are**  
629 **independent of locomotion.**

630 (A) Representative traces and boxplots reporting increase in speed (Looming  
631 on vs Looming off; 11 vs 11;  $4.1 \pm 0.56$  vs  $3.3 \pm 0.28$  pixel/frame;  $t_{20}=1.28$ ,  
632  $p=0.21$  Unpaired t-test) and the relative LHb activity (Looming on vs Looming  
633 off; 11 vs 11,  $1.19 \pm 0.02$  vs  $1.00 \pm 0.012$  normalized photon;  $t_{20} = 7.35$ ,  
634  $***p < 0.0001$  Unpaired t-test) in presence or absence of the looming stimulus.

635 (B) Same as (A) but for decrease in speed (Looming on vs Looming off; 10 vs  
636 10;  $-0.7558 \pm 0.10$  vs  $-0.9987 \pm 0.176$  pixel/frame;  $t_{18}=1.190$ ,  $p=0.249$   
637 Unpaired t-test) and relative LHb photon change (Looming on vs Looming off;  
638 10 vs 10,  $0.9204 \pm 0.014$  vs  $0.9807 \pm 0.007$  normalized photons;  $t_{18}=3.61$ ,  
639  $**p=0.002$  Unpaired t-test).

640 For this comparison, we selected the first runaway and action locking  
641 response for each mouse. Then we looked for a single episode outside  
642 looming presentation with a comparable change in speed for the same  
643 mouse. Note that one mouse did not display any action locking response  
644 throughout the recording session.  
645 Data are presented with boxplots (median and 10-90 quartile) or mean  $\pm$   
646 S.E.M.

647

648 **Figure 3—figure supplement 1. Opposite threat-driven responses occur**  
649 **in the same LHb neuronal ensemble**

650 (A) Mean  $\text{Ca}^{2+}$  responses for runaway (left) and action-locking (right) trials  
651 time-locked with the behavioral onset, including all cells recorded in 4 mice  
652 (n=248). Cells are sorted for response magnitude in runaway trials.  
653 On the bottom, runaway- and action-locking-locked averaged signals. Data  
654 are reported as z-score.  
655 (B) On the top, heat-map showing the cell distribution in the different  
656 categories according to their response to runaway and action-locking  
657 (Runaway/Action-locking: excited/inhibited=73, excited/non responsive=47,  
658 excited/excited=4, non responsive/inhibited=62, non responsive/non  
659 responsive=35, non responsive/excited=16, inhibited/inhibited=6,  
660 inhibited/non responsive=4, inhibited/excited=3). On the bottom, correlation  
661 analysis of single cell average  $\text{Ca}^{2+}$  responses (z-score) to runaway vs action  
662 locking displaying variability (Runaway vs Action-locking;  $n_{\text{cells}}=248$ ,  $r=-0.208$ ;  
663  $R^2=0.043$ ;  $***p<0.0001$ , Pearson correlation coefficient).  
664 (C) Top: Raster plots showing active (red squares) and non-active cells

665 (black squares), imaged over different runaway trials in a single mouse. On  
666 the right, the boxplot reports single cell reliability (%) for runaway responses  
667 ( $n_{\text{cells}}=248$ , Runaway,  $38.01 \pm 1.3 \%$ ). Bottom, same mouse as top. Raster  
668 plots showing cells inhibited (red squares) or not (black squares), imaged over  
669 different action-locking trials. On the right, the boxplot show reliability for  
670 single cells in percentage for action-locking reposes ( $n_{\text{cells}}= 248$ , Action-  
671 locking,  $32.71 \pm 1.37\%$ ).

672

673 **Figure 3—figure supplement 2. Cluster detection and topography during**  
674 **runaway and action-locking**

675 (A) Plot of the percentage variance explained per principal component,  
676 showing the number of principal components retained (dashed line).

677 (B) Individual retained principal components, showing response vectors to  
678 both runaway and action-locking trials.

679 (C) The graph reports the percentage of cells in each cluster (Cluster 1 to 8,  
680 number of cells per cluster: 26, 30, 22, 33, 28, 35, 29, 45) and single-mouse  
681 contribution per cluster (Cluster 1 to 8, number of cells per cluster. Mouse 1:  
682 16, 10, 0, 7, 3, 6, 7, 3. Mouse 2: 4, 4, 12, 8, 9, 22, 5, 10. Mouse 3: 4, 9, 0, 8,  
683 1, 1, 0, 4. Mouse 4: 2, 7, 10, 10, 15, 6, 17, 28).

684 (D) Topographical distribution of the clusters in LHb (action-predictive vs  
685 action-decoding clusters; rostral vs caudal cell distribution; Action-predictive:  
686 57 cells, 9 rostral vs 48 caudal. Action-decoding: 191 cells, 83 rostral vs 108  
687 caudal.  $X^2= 14.4$ ;  $z=3.79$ ;  $***p=0.0001$ , Chi-Square test).

688

689

690 **Material and methods**

691 **Experimental subjects**

692 The experiments were performed on C57Bl/6J mice wild-type males of 10-18  
693 weeks. Mice were housed at groups of five per cage with water and food ad  
694 libitum on a 12:12 h light cycle (lights on at 7 a.m.). All procedures aimed to  
695 fulfill the 3R criterion and were approved by the Veterinary Offices of Vaud  
696 (Switzerland; License VD3171).

697

698 **Behavioral paradigm**

699 Mice were tested for behavior in a looming visual stimulus test, as described  
700 elsewhere (Yilmaz and Meister, 2013). Animals were placed in an open-top  
701 plexiglas box (58cm Lx 38cm Wx 32cm H). A triangular shaped nest (20 × 12  
702 cm) was placed in one corner. Recordings were performed under illumination  
703 provided by the projector screen (52 cm × 30 cm; Dell) and an infrared light-  
704 emitting diode (LED) illuminator (Pinnacle Technology), both placed above the  
705 arena. Experiments were recorded at 60 frames per second with a near-IR  
706 GigE camera (acA1300-60gmNIR, Basler) positioned in one side of the arena.  
707 Video recording, was controlled with Ethovision and synchronized with the  
708 photometric and endoscopic recordings using hardware-time signals  
709 controlled with a I/O box (Noldus). All the mice tested underwent a period of  
710 habituation to the fiber/camera spanning from 15-20 min session every day for  
711 3 consecutive days. For the experiment, after 5-10 min of acclimatization, a  
712 looming stimulus (always delivered at 50% contrast), was randomly presented  
713 from the screen in the center of the arena while the mouse was actively  
714 exploring (independently by its position in the arena). The stimulus of 0.5 s

715 duration was repeated 5 times with an inter-stimulus interval of 0.5 s. Each  
716 mouse received from 7 to 20 trials with a minimum inter-trial interval of about  
717 5 minutes. The video analysis of the behavior was performed off-line.

718

719 *Automated detection of mouse shape and position.* A fully convolutional  
720 neural network was used to extract the shape of the mouse across the arena.  
721 Each video (1920 x 1088 @ 60 fps) was converted to a sequence of images  
722 (8-bit, 256 x 144 pixel). The training dataset was composed of 112 images  
723 and it was used to trace a set of 112 masks (8-bit, 256 x 144 pixel binary  
724 images) delineating the contour of the mouse body and to output the files  
725 storing the coordinates of the center of mass of each individual mask. Each  
726 image in the training dataset was passed through three convolutional layers  
727 (channels: 16, 32, 64; kernels: 3, 5, 3, stride: 1, ReLU units), two max-pooling  
728 operations (kernel size: 2), and three transposed convolutional layers. The  
729 frames were processed in batches of 64 images for 171 epochs). The network  
730 was built with the open source library PyTorch 1.2 (<https://pytorch.org/>) and  
731 trained to minimize (Adam optimizer, learning rate: 0.003) the Mean-Squared  
732 Error loss function. Accuracy was measured as the Euclidean distance  
733 between the centroid of the mask of the training set and the centroid of the  
734 score map predicted by the network. An arbitrary cutoff was used to define  
735 the boundaries of the estimated mouse shape on the score map. The mean  
736 accuracy on the test set was 1.65 px (+/- 1.51 px, standard deviation), with  
737 96.4% of the frames showing a distance between centroids (i.e. label Vs  
738 predicted) less than 7 px. The output coordinates of the center of mass were  
739 then used to compute the speed (pixels/seconds) and the location of the



740 mouse inside the arena. The onset of runaway was measured as the peak of  
741 the first derivative of the mouse speed tracking curve. The runaway offset was  
742 coinciding with the mouse entrance in the nest. The score map was used to  
743 estimate the size of the mouse (e.g. total number of pixel above the arbitrary  
744 threshold) across the arena and used for further calculations to score action-  
745 locking behavior.

746

747 *Automated classification of action-locking behavior.* An observer blind to the  
748 experimental condition of the animals manually scored the action locking  
749 behavior, defined as a sudden blockade of all -except respiratory-  
750 movements. In contrast to freezing, action locking was not associated with a  
751 particular body posture (i.e. crouching). The sudden immobility had to last at  
752 least two seconds in order to score the animal as actively producing an  
753 action-locking behavior. Data obtained from the manually labeled frames were  
754 then merged with the data (speed and size) obtained from the automatic  
755 detection of the mouse position to train a random forest classifier to predict in  
756 each frame whether the animal was in action-locking. Both speed and size  
757 were convolved with a Max function (window = 60 frames) and a total of four  
758 features were used: speed (v), size (s), es, and ev. A 5-fold cross-validation  
759 yielded an overall accuracy of 98%. The accuracy achieved on the test set  
760 was 97.5% with a false positive rate of 2.6%.

761

## 762 **Surgical procedures**

763 *Viral injections.* All mice were anaesthetized with ketamine (150  
764 mg/kg)/xylazine (10 mg/kg) (Sigma-Aldrich, France). We unilaterally injected

765 in the LHb (-1.4 mm AP, 0.45 ML, 3.1 mm DV) rAAV2.1-hSyn-GCaMP6f-  
766 eGFP or rAAV/DJ-hSyn- -GCaMP6f-eGFP or rAAV2.5-hSyn-eGFP (University  
767 of North Carolina, US) using a glass pipette on a stereotactic frame (Kopf,  
768 France). Volumes ranged between 200 and 300 nl, at a rate of approximately  
769 100-150 nl/min. The injection pipette was withdrawn from the brain 10 minutes  
770 after the infusion. Animals were allowed to recover for a minimum of two  
771 weeks before fiber or GRIN lenses implantation.

772

773 *Chronic implants.* For fiber photometry experiments, a single fiber probe was  
774 placed and fixed (C and B Metabond, Parkell) 150  $\mu\text{m}$  above the injection site  
775 in isoflurane anesthetized (induction: 4%, maintenance: 1.8-2%) mice.  
776 For endoscope experiments, mice were anaesthetized (as described above)  
777 and implanted with a GRIN (Graded-Index) lens (6.1mm length, 0.5mm  
778 diameter; Inscopix, #100-000588). The lens was targeted to be ~ 150–200  $\mu\text{m}$   
779 above the injection site using the following coordinates: -1.40 mm posterior to  
780 bregma, 0.45 mm lateral from midline, and -2.85 to -2.9 mm ventral to skull  
781 surface (lowered at a speed of 1 $\mu\text{m/s}$ ). To increase stability of the implants  
782 the lenses were implanted into the dorsal portion of the region allowing  
783 imaging ventral LHb neurons. Two week after lens implantation, mice were  
784 again anaesthetized (isoflurane, as above) and a baseplate (Inscopix, #100-  
785 000279) was secured above the lens. A baseplate cover (Inscopix, #100-  
786 000241) was attached to prevent damage to the microendoscope lens. Out of  
787 23 mice that were injected with GCaMP6f virus, 4 had successful lens  
788 implantation/viral expression and were used for this study.

789

## 790 **Fiber photometry recordings**

791 Fiber photometry measurements were carried out by the ChiSquare X2-200  
792 system (ChiSquare Biomaging, Brookline, MA). Briefly, blue light from a 473-  
793 nm picosecond-pulsed laser (at 50 MHz; pulse width ~ 80 ps FWHM) was  
794 delivered to the sample through a single mode fiber. Fluorescence emission  
795 from the tissue was collected by a multimode fiber with a sample frequency of  
796 100Hz. The single mode and multimode fibers were arranged side by side in a  
797 ferrule that is connected to a detachable multimode fiber implant. The emitted  
798 photons collected through the multimode fiber pass through a bandpass filter  
799 (FF01-550/88, Semrock) to a single-photon detector. Photons were recorded  
800 by the time-correlated single photon counting (TCSPC) module (SPC-130EM,  
801 Becker and Hickl, GmbH, Berlin, Germany) in the ChiSquare X2-200 system.

802

## 803 **Endoscope recordings**

804 All calcium imaging was recorded at 20 frames per second, 200-ms exposure  
805 time, and 10–40% LED power (0.4-0.9mW at the objective, 475nm) using a  
806 miniature microscope from Inscopix (nVista). Calcium recording files were  
807 down-sampled (spatial binning factor of 4) to reduce processing time and file  
808 size, filtered, corrected for rigid brain movement and the  $\Delta F/F_0$  was  
809 calculated using as  $F_0$  the average fluorescence for all the video (Inscopix,  
810 IDP). Individual component analysis and principle component analysis  
811 (ICA/PCA) applications were used to identify individual cells and to extract  
812 their respective calcium traces.

813 In addition, to compare ROI detections and relative traces obtained with the  
814 PCA/ICA we also performed constrained non-negative matrix factorization for

815 endoscopic data (CNMF-E) for a subset of data. Briefly, we denoised,  
816 deconvolved, and demixed calcium-imaging dynamics  
817 ([http://www.github.com/zhoup/cnmf\\_e](http://www.github.com/zhoup/cnmf_e)). This method allows accurate single  
818 neurons fluorescence traces extraction (Zhou et al. 2018). Calcium imaging  
819 frames were initially pre-processed in Mosaic (Inscopix) for motion correction.  
820 We use a Gaussian kernel width 4  $\mu\text{m}$ , maximum soma diameter 16  $\mu\text{m}$ ,  
821 minimum local correlation 0.8, minimum peak-to-noise ratio 8 and merging  
822 threshold was set to 0.65 for optimal discrimination of temporal and spatial  
823 overlap.

824

## 825 **Analysis**

826 Photometric signal as well as ICA/PCA derived traces were smoothed  
827 (constant time factor, 0.1 s) and further processed according to the trials using  
828 Spike2 software (Cambridge Electronic Design). We obtained an average  
829 peri-stimulus time histogram (PSTH) trace aligned to the stimulus or  
830 behavioral onset/offset (3 s prior and 7 sec after a given event). For the  
831 photometric recordings we calculate the photon change normalizing for the 3  
832 sec prior each trial. For the endoscope recordings we z-scored each trials in  
833 reference to their baseline (3 s prior to behavior onset).

834 We identified functional sub-classes of neurons by comparing the  
835 fluorescence  $\text{Ca}^{2+}$  signals of individual cells before and after a given event,  
836 using 2s time span. For runaway trials we consider a cell excited if the signal  
837 2 s post runaway onset was higher than the baseline plus 2 SD. Vice versa a  
838 cell was inhibited if its signal in the 2s post runaway resulted 2 SD lower than  
839 their baseline. For action-locking responses we considered 3 epochs (2s each

840 epoch) of analysis post event according with the average duration of this  
841 behavior (6s). If the signal in at least one epoch resulted higher or lower than  
842 2 SD of the baseline the cell was considered action-locking excited or  
843 inhibited respectively.  
844 For the analysis of the single trials we follow the same logic above-mentioned  
845 except that the epochs considered for the action locking were updated each  
846 time according with the duration of the response.

847

### 848 **Clustering and decoding**

849 For clustering neurons based on their average responses around action onset  
850 for both action-locking and runaway trials, we followed a similar general  
851 procedure as in Namboodiri et al. 2019. Briefly, we first calculated the  
852 average peri-event time histogram (PETH) for each neuron around each  
853 action by averaging all trials. Due to the variability in reaction times from  
854 looming stimulus onset until the action, we calculated the PETHs around a  
855 time window from -0.5 s to +7s surrounding the action. This ensured that only  
856 activity after the looming stimulus onset was included in all trials. The PETH  
857 surrounding both action-locking and runaway trials were treated as features of  
858 the response of a neuron. This feature space was then reduced in  
859 dimensionality using principal components analysis (Fig S5). The number of  
860 principal components to keep was decided based on the bend in the scree  
861 plot (Namboodiri et al. 2019). A spectral clustering algorithm along with  
862 optimal selection of number of clusters using silhouette scores (Namboodiri et  
863 al. 2019) was used on the principal component scores to test for presence of  
864 clusters. The number of clusters was chosen by maximizing the silhouette

865 score. Once cluster identities were assigned, all PETHs were recalculated  
866 using the activity from -3 s to +7 s surrounding the actions. Only activity  
867 following looming stimulus onset was included. If the looming stimulus onset  
868 was less than 3 s prior to action on a trial, these data were treated as “not a  
869 number (nan)” in our analysis pipeline.

870

871 We then tested for significant decoding by analyzing whether the activity of a  
872 single neuron could be used to decode the chosen behavioral action on a trial.  
873 To calculate a decoding accuracy, we trained a Naïve Bayes classifier on all  
874 but one trial (leave-one-out cross-validation) and tested the decoding  
875 accuracy on the remaining trial for each time epoch (Figure 4B). Within each  
876 epoch, three “response features” were used for decoding analysis: slope of  
877 the linear fit to fluorescence within the epoch, y-intercept of this fit, and lastly,  
878 the standard deviation of fluorescence within the epoch (Figure 4B). Only  
879 three features were used to avoid overfitting and maximize generalizability of  
880 decoding on test trials. This procedure was repeated with each trial as the test  
881 trial, to obtain an overall decoding accuracy above chance accuracy obtained  
882 by shuffling trial identity. For the shuffled null, we calculated the mean chance  
883 accuracy per neuron as the mean accuracy across ten different shuffles. We  
884 applied this procedure to one neuron at a time to obtain a decoding accuracy  
885 per neuron, which was then averaged across all neurons recorded, or all  
886 neurons within a cluster. The decoding accuracy above chance was simply  
887 calculated as the difference in population mean between the true accuracies  
888 and the shuffled accuracies. Significance was tested based on a two-sample  
889 t-test between the true accuracies and the shuffled accuracies.

890 **Statistical analysis.**

891 Offline analyses were performed using Prism 8 (Graphpad, US). Single data  
892 points are always plotted. Sample size was pre-estimated from previously  
893 published research and from pilot experiments performed in the laboratory.  
894 Each mouse represents an analytical unit, for each experiment we stated the  
895 replication factor. Compiled data are expressed as boxplots (median and  
896 quartiles) or mean  $\pm$  S.E.M. Significance was set at  $p < 0.05$  using two-sided  
897 unpaired t-test, one or two-way ANOVA. Correlational analysis was performed  
898 with Pearson test. Frequency distribution was analyzed with  $\chi^2$  test. The use  
899 of the paired t-test and two way ANOVA for repeated measured were stated in  
900 the legend figure text.

901

902

903

904

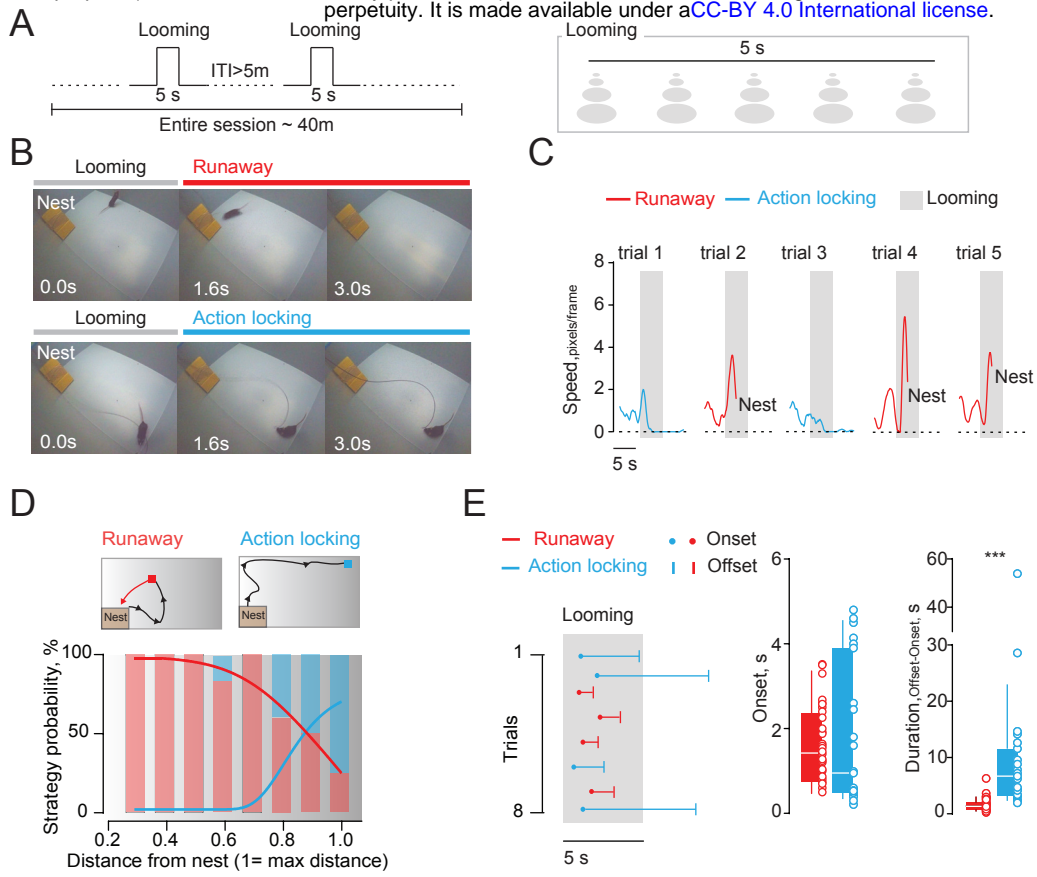
905

906

907

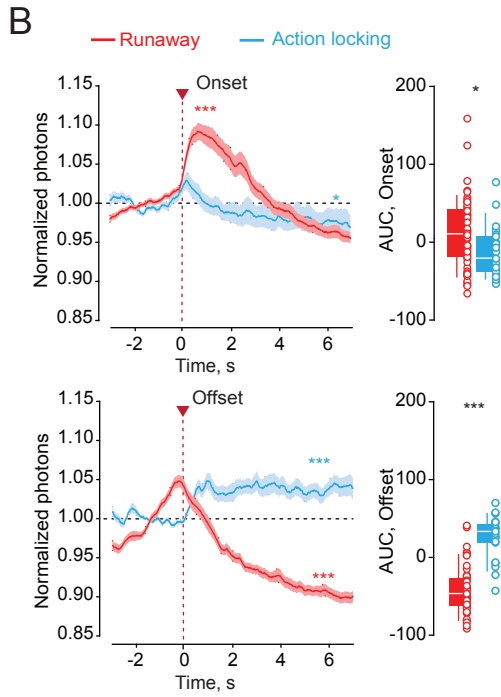
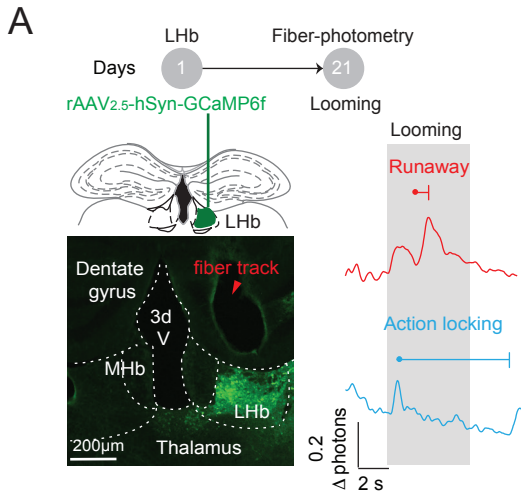
908

909

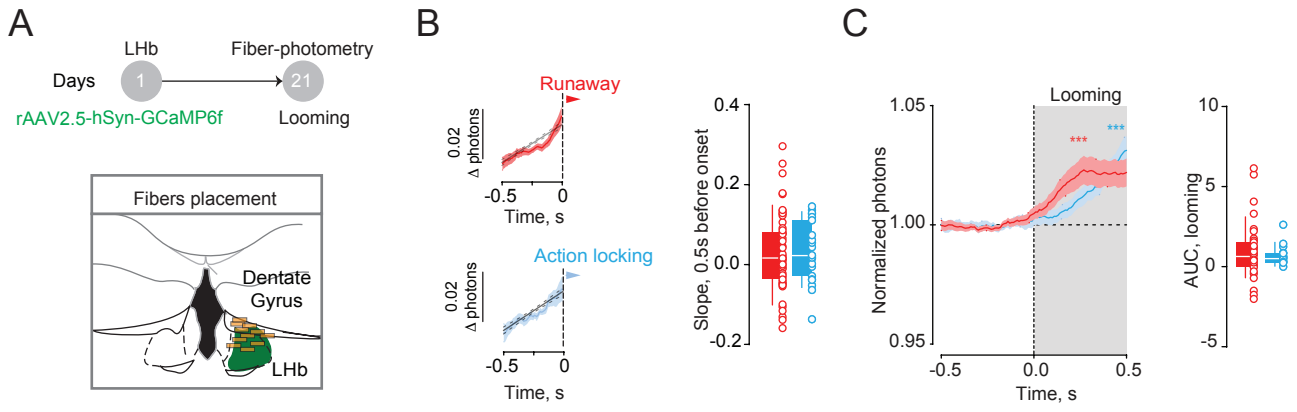


Lecca et al., Figure 1



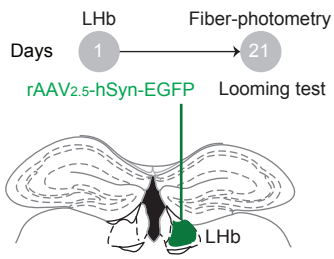


Lecca et al., Figure 2

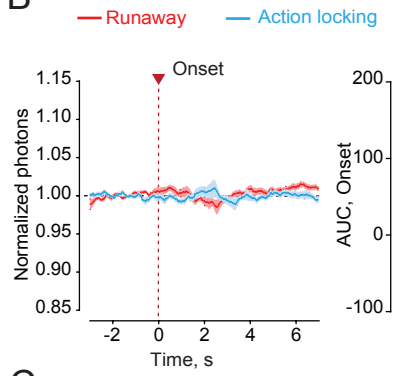


Lecca et al., Figure 2-supplement 1

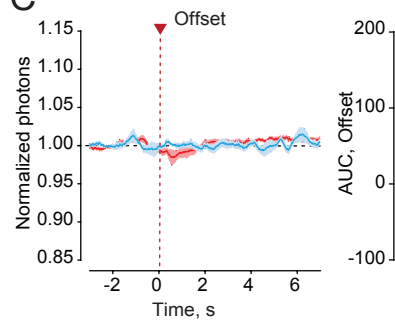
**A**

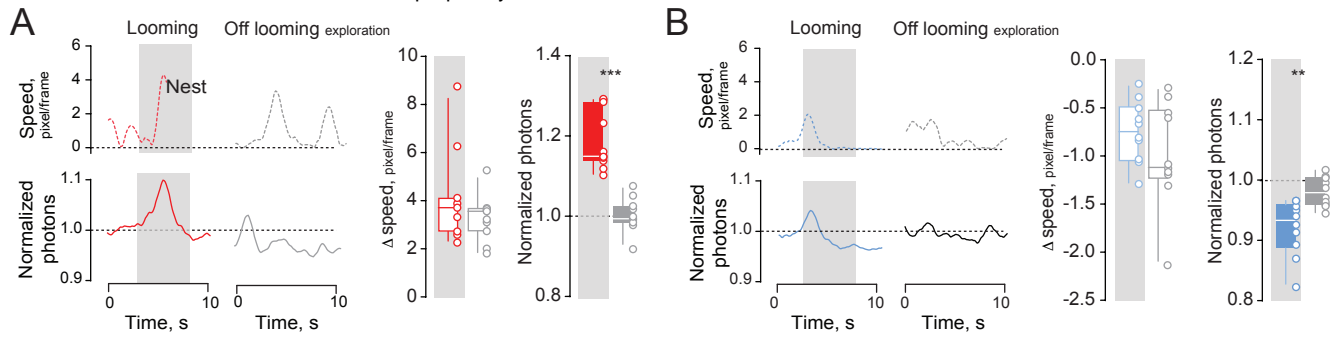


**B**



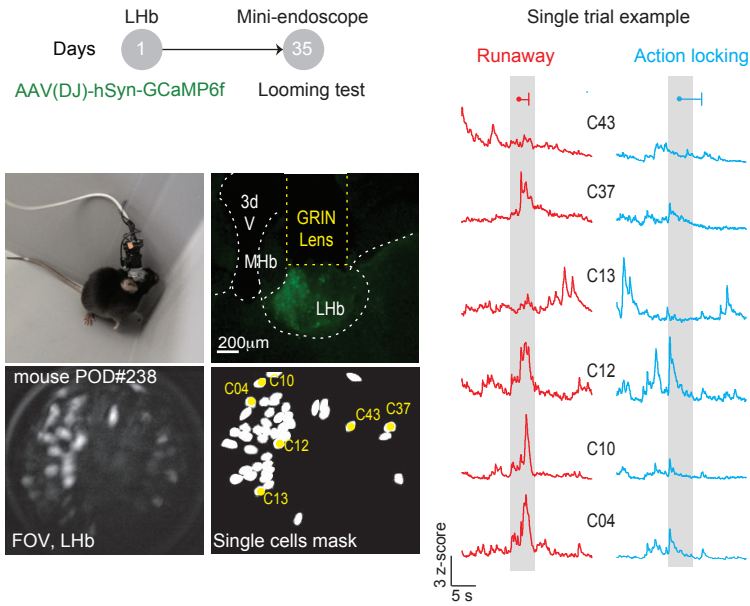
**C**



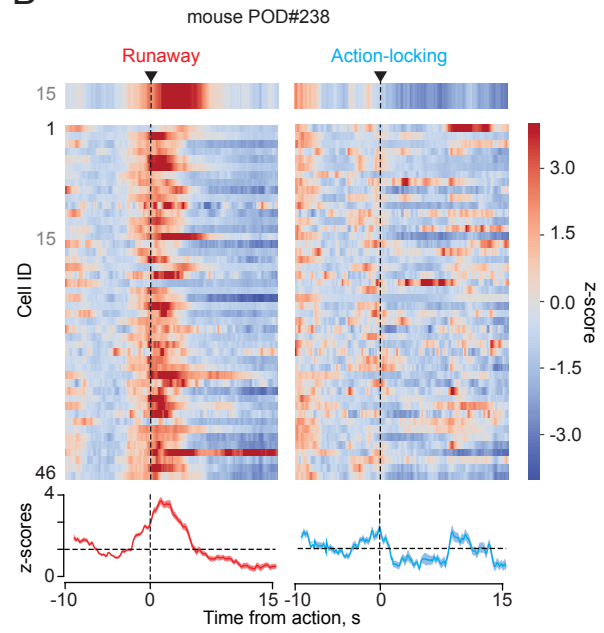


Lecca et al., Figure 2-supplement 3

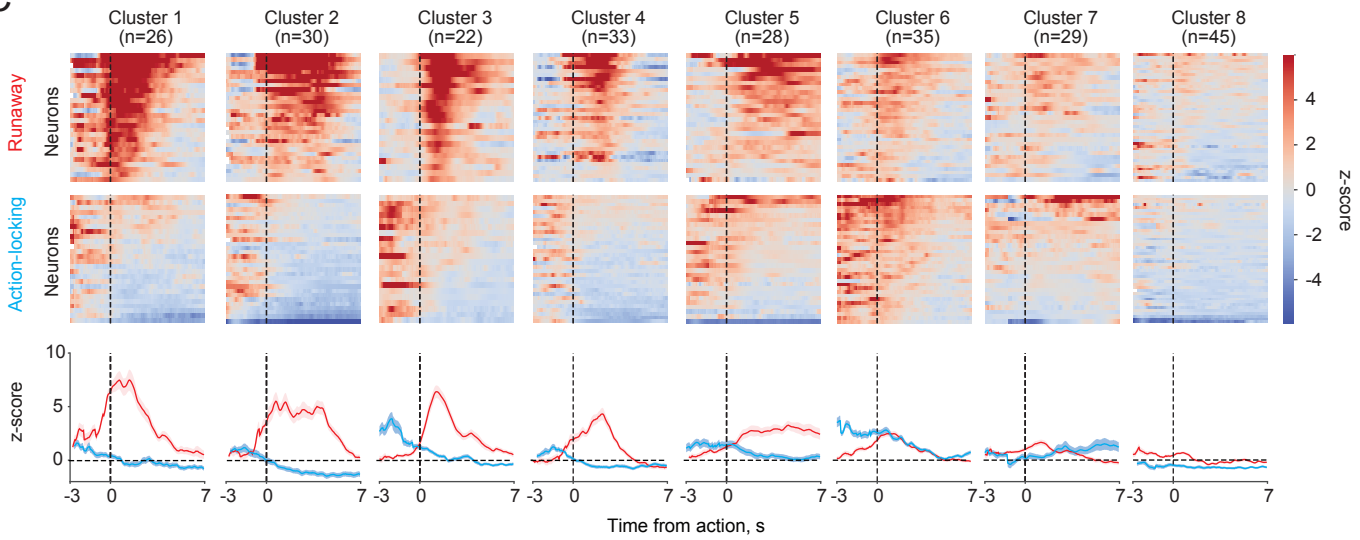
A



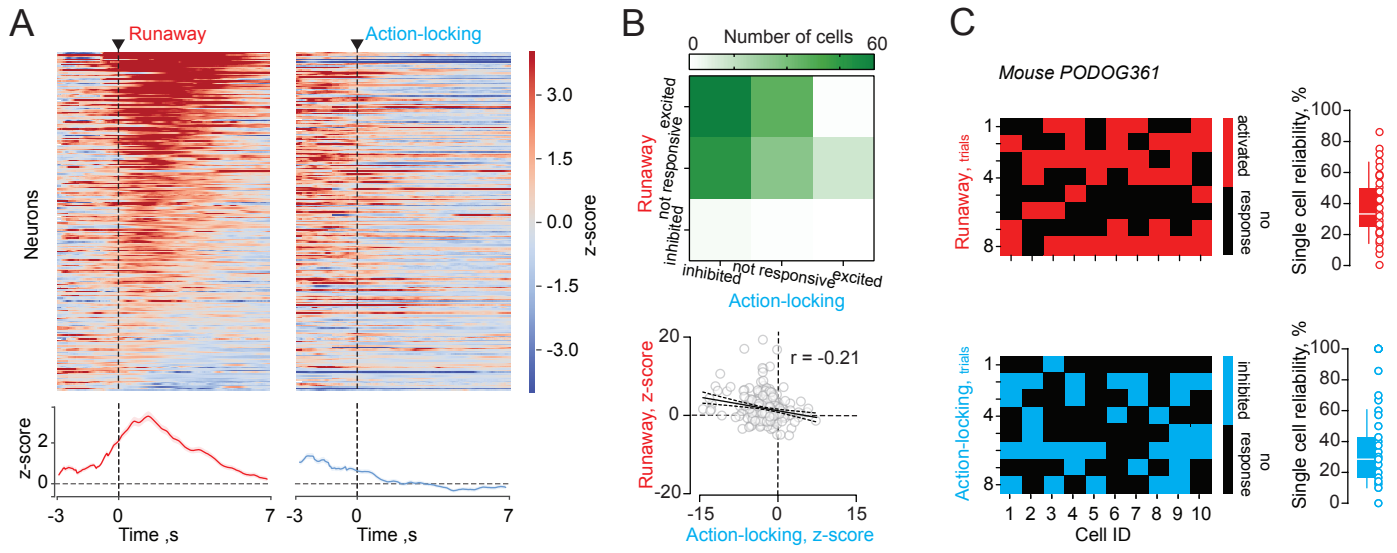
B



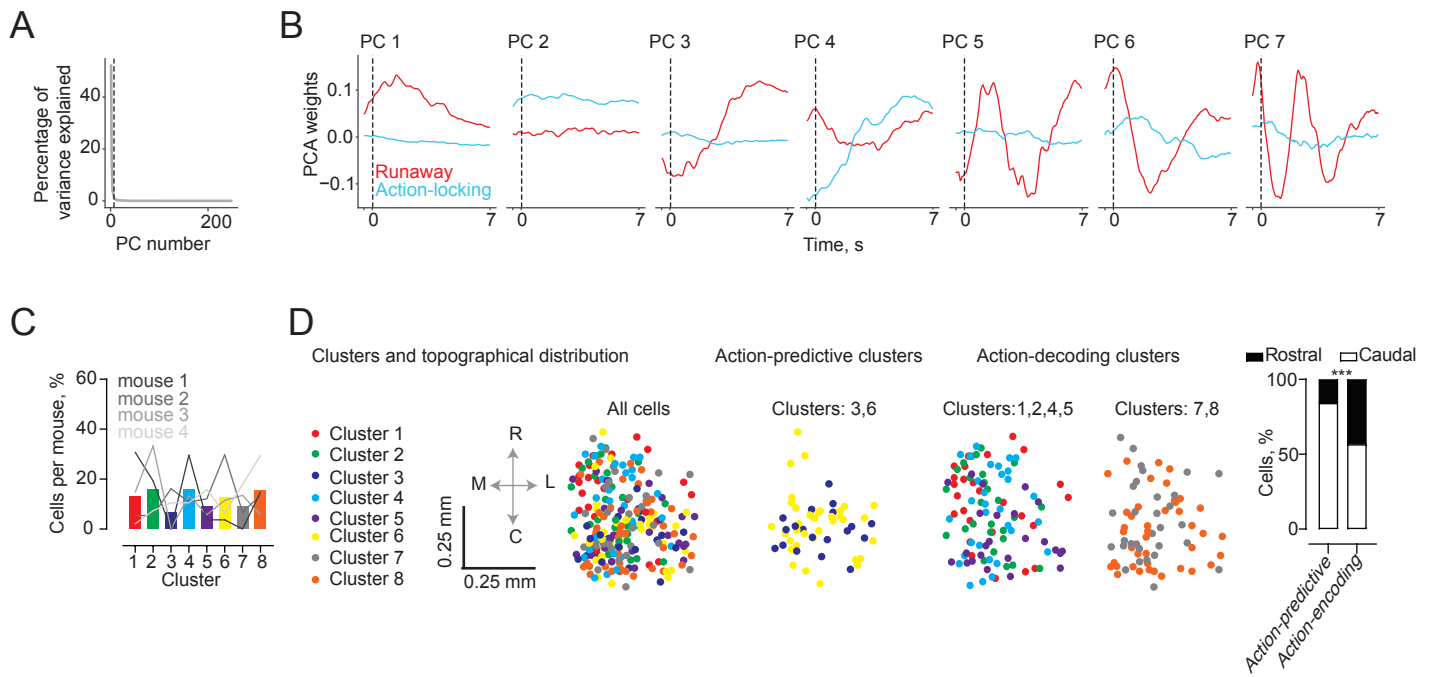
C



Lecca et al., Figure 3

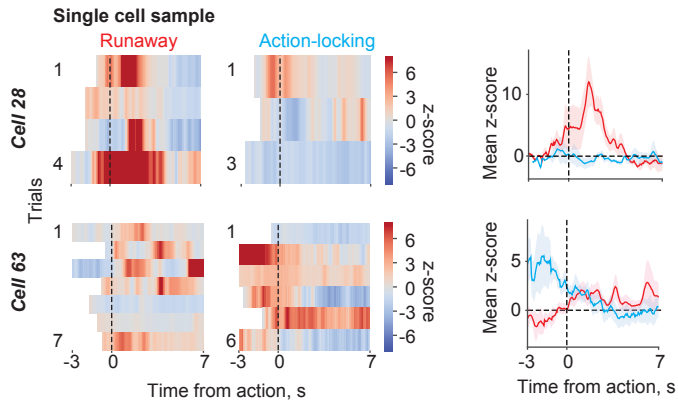


Lecca et al., Figure 3-supplement 1

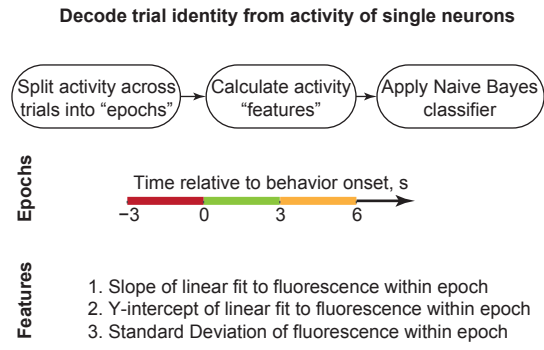


Lecca et al., Figure 3-supplement 2

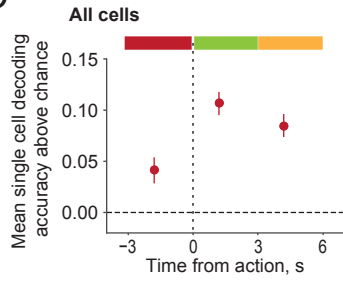
A



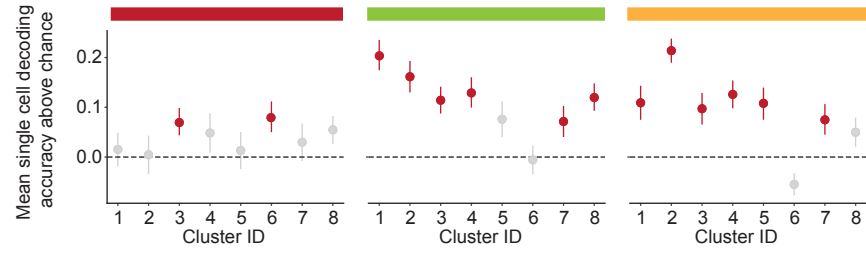
B



C



D



Lecca et al., Figure 4